This is a Just Accepted version, keep updated with https://doi.org/10.26599/LLES.2026.9660017

Research Article

Study on the oxygen availability of steel corrosion in concrete based on a heat-moisture-chlorine-oxygen multi-field coupled transport model

Guo-Yi Zhang[1], Ye Tian[2, ✉], Zu-Shi Tian[3], Ke-Wei Yu[4]

[1] *College of Landscape Architecture, Zhejiang A&F University, Hangzhou 310058, China*

[2] *Department of Civil Engineering and Architecture, Zhejiang University, Hangzhou 310058, China*

[3] *Department of Civil Engineering, The University of Hong Kong, Hong Kong, China.*

[4] *College of Landscape Architecture, Zhejiang A&F University, Hangzhou 310058, China*

✉ Address correspondence to Ye Tian, cetianye@zju.edu.cn

Received: 25 December 2025; Revised: 30 January 2026; Accepted: 02 March 2026

ABSTRACT

Oxygen availability governs the cathodic reactions during the corrosion propagation stage. However, existing studies often neglect the coupled effects of heat, moisture, chloride, and oxygen transport, leading to inaccurate predictions of corrosion rates. This study developed a multi-field coupled model that integrates heat-moisture transfer, chloride transport, and oxygen diffusion-consumption dynamics to investigate the role of oxygen availability in steel corrosion. Accelerated corrosion tests were conducted under cyclic temperature conditions of 20~40℃ and humidity levels of 40~80% to monitor key parameters, including oxygen concentration, chloride ions distribution, and corrosion current density. Results reveal that due to cathodic consumption, the oxygen concentration at the steel surface is significantly lower than that in the surrounding concrete. High temperature and humidity reduce oxygen availability by limiting diffusion and solubility, while chloride ions accelerate depassivation and indirectly influence oxygen consumption. A sharp decline in oxygen concentration, coupled with a rise in corrosion current density, was observed before and after steel depassivation.

KEYWORDS

Steel corrosion; oxygen availability; multi-field coupling; transport and consumption equilibrium; accelerated corrosion under dry-wet cycles; finite element simulation.

1. Introduction

The corrosion of steel rebars poses a challenge to the longevity and strength of reinforced concrete structures, particularly when exposed to marine environments. Steel corrosion induced by chloride ions includes two main stages, the initiation stage and the propagation stage[1]. During the initiation phase, the accumulation of chloride ions leads to the depassivation of the steel[2]. Sufficient supply of oxygen on the steel surface accelerates the transition from the initiation stage to the propagation stage, thereby increasing steel corrosion rate[3]. When corrosion products are formed, they generate internal pressure at the steel-concrete interface, leading to cracking and spalling of concrete, and severely affecting the service performance of structures[4]. Therefore, the availability of oxygen during steel corrosion process significantly affects the durability and safety of reinforced concrete structures.

Recognizing the crucial role of oxygen in the steel corrosion process, numerous researchers have engaged in extensive theoretical modeling and experimental investigations[5, 6]. The existing theoretical frameworks mainly focus on the electrochemical reaction polarization principles related to steel corrosion, along with the mechanisms underlying microcell and macrocell corrosion. These models are designed to offer predictive insights into steel corrosion rate [7, 8]. For instance, Cao developed an electrochemical model to predict non-uniform steel corrosion induced by chloride ions, revealing that the ratio of cathodic to anodic areas positively influences the severity of macrocell corrosion[9]. Similarly, Yu identified a critical level of humidity, suggesting that prior to reaching this threshold, increases in humidity can enhance the corrosion rate of steel, while exceeding this level may actually reduce the rate due to restricted oxygen access caused by excessive moisture[10]. On the experimental front, steel corrosion is often evaluated through measurements of corrosion reaction rates and the mechanical properties of affected steel rebars. Otieno performed accelerated corrosion tests on beam specimens using a

cyclic wetting and drying method, finding the corrosion behavior of concrete observed in natural environments cannot be reliably predicted from results obtained under accelerated laboratory conditions[11].

Most studies only focus on the impact of single factors on steel corrosion, lacking systematic analysis under multi-field coupling effects. Existing steel corrosion models mainly emphasize the impact of chloride ions, frequently neglecting the critical role of oxygen[12]. While some research acknowledges the importance of oxygen, conflicting findings indicate a need for further exploration. From an electrochemical standpoint, the presence of oxygen within the cathodic region plays a pivotal role in influencing the propagation stage of corrosion[13]. Yu's research further demonstrated the corrosion rate of steel embedded in concrete initially accelerates and subsequently declines with increasing relative humidity[10]. This observed pattern can be attributed to diminished oxygen availability for the cathodic reactions at elevated humidity levels. Thus, a specific threshold for relative humidity exists, leading to a shift in the mechanisms controlling corrosion from the anodic reaction (governed by chloride ions) to the cathodic reaction (influenced by oxygen). Although these investigations have underscored the role of environmental factors in determining steel corrosion rates, there remains a significant gap in comprehensive studies examining how oxygen precisely regulates the steel corrosion rates.

To reduce the difficulty of analyses, previous studies often equaled the temperature and humidity of the macro environment to those at the steel surface, and make them as the foundation for calculating medium transport. Consequently, these research findings frequently exhibit substantial discrepancies[14, 15]. There are notable distinctions between the micro-environment at the steel surface and the macro-environment surrounding the structure[16]. The physical and chemical interactions occurring in the micro-environment on steel-concrete interface are crucial in influencing the corrosion rate[17]. To gain deeper insights into the interaction between external and internal concrete environments, researchers have employed multi-field coupling theory to investigate the transfer mechanisms of heat and moisture in concrete[18]. For instance, Gawin developed macroscopic mass balance equations to characterize the coupled heat and moisture transfer processes in the concrete microstructure[19]. However, despite these advancements, there remains a lack of studies that apply multi-field coupling theory specifically to the exploration of

steel corrosion in micro-environments.

The distribution of oxygen concentration on steel surface is regulated by two main processes: transport and consumption. The transport of oxygen is affected by various concrete properties, such as the mix design, type of cementitious materials used, and the presence of any admixtures[20]. Moreover, the distribution pattern of humidity within the concrete matrix significantly affects the oxygen transport performance. Oxygen consumption rate is primarily determined by cathodic reaction. The presence of chloride ions on the steel surface plays a crucial role in determining the intensity of the current cycle between the anode and cathode in the macrocell, ultimately affecting oxygen consumption rate in the cathodic region. Moreover, oxygen primarily migrates through concrete in its gaseous state, whereas its consumption within the pore solution occurs in its dissolved form. Rettich utilized Henry's law constant to describe the solubility of oxygen, emphasizing the equilibrium between gaseous and dissolved oxygen is influenced by temperature[21].

Many experimental studies on steel corrosion applied galvanic accelerated corrosion techniques to obtain corroded steel. For example, Zhang concluded applied current intensity affects the composition of corrosion products[22]. However, the electrochemical mechanisms that drive current-accelerated corrosion differ markedly from those in natural corrosion, particularly regarding cathodic and anodic reactions. As a result, findings obtained through electric acceleration methods often do not align with observations made under natural environmental conditions[23]. To bridge this gap, some researchers have attempted to replicate the temperature, humidity, chloride ions concentration, and other environmental factors typical of natural settings within laboratory conditions, conducting accelerated corrosion tests under controlled climate conditions. Zhao, for instance, conducted dry-wet cycle accelerated corrosion tests to investigate the variation in rust layer thickness distribution[24]. Despite these initiatives, most current research tends to concentrate on individual variables, such as corrosion current density or the morphology of rust layers. There is often a lack of comprehensive and systematic monitoring of crucial parameters, including temperature, humidity, oxygen, and chloride ions concentration, within the concrete microenvironment throughout the corrosion process[11]. This gap limits the understanding of the dynamic corrosion process.

This study developed an electrochemical model to explore the connection between oxygen availability and steel corrosion in the cathodic region. The model integrates heat, moisture, chloride ions, and oxygen transport, addressing their interactions and oxygen diffusion-consumption dynamics. Using electrochemical polarization equations and microcell-macrocell models, a finite element model was created. Accelerated corrosion tests under varying conditions monitored temperature, humidity, oxygen, chloride ions concentrations, and corrosion current density, enabling a systematic analysis of their influence on oxygen availability in the cathodic region.

2. Corrosion model of steel under coupled heat-moisture-chlorine-oxygen transport

2.1 Coupled heat and moisture transfer

Under natural marine environment, climatic conditions undergo annual cyclical variations, leading to the non-uniform transfer of heat and moisture over time[16]. The coupled behavior of heat and moisture within concrete results in the non-uniform distribution of oxygen and chloride ions, subsequently impacting the rate of steel corrosion. To effectively investigate how oxygen supply in the cathodic region influences the corrosion rate of steel, it is essential to account for the coupled transfer of heat and moisture in concrete. However, many previous studies have simplistically equated the heat and moisture of the external environment with those within the concrete itself. This assumption introduces discrepancies between the calculated results and real-world conditions. In light of this, the current study addresses this issue by incorporating factors such as heat, moisture, and dry air, and develops a new model for heat-moisture coupling transfer. To balance model simplicity and reliability, we adopt key assumptions for the multi-field coupling framework. Concrete is treated as a homogeneous porous medium with isotropic physical and mechanical properties, and chemical reactions between concrete components and external ions are ignored except for chloride ion binding.

2.1.1 Mass and energy conservation equations

Based on the Hybrid Mixture Theory[25], concrete consists of a solid skeleton, liquid water, and gas. Solid phase (subscript S for short, the same below) mainly consists of aggregates and unhydrated cement. Liquid water (L) mainly includes pore solution. Gas phase (G) consists of dry air (A) and water vapor (V). The macroscopic mass and energy conservation equations for π phase

(π=*S*, *L*, *G*, *A*, *V*) in concrete are as follows[26]:

$$\frac{D\left(\varepsilon_S \rho_S\right)}{Dt} + \varepsilon_S \rho_S \nabla \cdot \mathbf{v}_S = \dot{M}_h \tag{1}$$

$$\frac{D\left(\varepsilon_L \rho_L\right)}{Dt} + \varepsilon_L \rho_L \nabla \cdot \mathbf{v}_L = -\dot{M}_{va} - \dot{M}_h \tag{2}$$

$$\frac{D\left(\varepsilon_G \rho_V\right)}{Dt} + \varepsilon_G \rho_V \nabla \cdot \mathbf{v}_G + \nabla \cdot \left(\varepsilon_G \rho_V \mathbf{u}_V\right) = \dot{M}_{va} \tag{3}$$

$$\frac{D\left(\varepsilon_G \rho_A\right)}{Dt} + \varepsilon_G \rho_A \nabla \cdot \mathbf{v}_G + \nabla \cdot \left(\varepsilon_G \rho_A \mathbf{u}_A\right) = 0 \tag{4}$$

$$\left(\rho C\right)_{eff} \frac{\partial T}{\partial t} - \nabla \cdot \mathbf{q} - \left(\varepsilon_L \rho_L C_L \mathbf{v}_L + \varepsilon_G \rho_G C_G \mathbf{v}_G\right) \cdot \nabla T = -\dot{M}_{va} \Delta H_{va} \tag{5}$$

where ε_π is volume fraction; ρ_π is the density; $\dot{M}_{va}$ is the evaporation rate of free water; $\dot{M}_h$ is the mass source of solid skeleton; $\mathbf{q}$ is the heat flow; C_π is constant pressure specific heat[27]; ΔH_{va} is the specific enthalpy of evaporation; $(\rho C)_{eff}$ is the effective heat capacity of concrete; $\mathbf{v}_\pi$ is the velocity; $\mathbf{u}_\pi$ is the diffusion rate.

2.1.2 Constitutive relationships

Constitutive relationships are adopted to model the thermodynamics of fluid transport in concrete, which will be described in detail next. As the first constitutive relation, the humidity adsorption curve defines the humidity transport characteristics of concrete[28]. For mature concrete with a stable microscopic pore structure, the Kelvin-Laplace equation establishes the correlation between capillary pressure and relative humidity under thermodynamic equilibrium conditions[29]:

$$\ln H = -\frac{P_C M_V}{\rho_L R T} \tag{6}$$

where H(%) is the relative humidity in concrete; T(K) is the temperature in concrete; P_C(Pa) is the capillary pressure; M_V=0.018(kg/mol) represents the molar mass of water; R=8.314J/(mol·K) is the universal gas constant.

Darcy's law is adopted as the second constitutive relation to describe the low-velocity convective flow behavior of fluid in concrete pores[18]:

$$\mathbf{J}_d^{\pi} = \varepsilon_{\pi}\rho_{\pi}\mathbf{v}_{\pi} = -\varepsilon_{\pi}\rho_{\pi}\frac{\mathbf{K}K_{\pi}}{\mu_{\pi}}\left(\nabla P_{\pi} - \rho_{\pi}\mathbf{g}\right) \tag{7}$$

where $\mathbf{J}_d^{\pi}$ is the diffusion flux; $\mathbf{K}$ represents the inherent permeability coefficient tensor of concrete[26]; K_{π} is the relative permeability coefficient[30]; μ_{π} is the dynamic viscosity coefficient[31]; $\mathbf{g}$(m^2/s) is the acceleration of gravity.

Fick's law is utilized as the third constitutive relationship to characterize the diffusion-driven mass transport of water vapor and dry air:

$$\mathbf{J}_d^{\pi} = -\varepsilon_G\rho_G\mathbf{D}_G\frac{M_A M_V}{M_G{}^2}\nabla\left(\frac{P_{\pi}}{P_G}\right) \tag{8}$$

where $\mathbf{J}_d^{\pi}$ denotes the diffusion flow. The effective diffusion tensor, $\mathbf{D}_G$, which is influenced by temperature and gas pressure, is assumed to be the same for both water vapor and dry air[32].

As the fourth constitutive relation, Fourier's law states that the heat flux is proportional to the temperature gradient, regulated by the effective thermal conductivity coefficient λ[33]:

$$q = -\lambda\nabla T \tag{9}$$

2.1.3 Control equations and boundary conditions

The primary variables to be solved in the model are temperature T, capillary pressure P_C, and mixed gas pressure P_G, which represent the states of heat, moisture, and gas mixture in the concrete, respectively. The control equations of the coupled heat-moisture transfer model in concrete are derived by integrating the mass and energy conservation equations with the constitutive equations, which are presented in **Appendix**. Since concrete structures are often exposed to time-varying environments, the boundary conditions for heat and moisture of the model also vary over time:

$$\left(-\lambda\nabla T\right)\cdot\mathbf{n} = h_T\left(T - T_{\infty}\right) \qquad on\ \ \Gamma_T^q \tag{10}$$

$$\left(\varepsilon_G\rho_V\mathbf{v}_G + \mathbf{J}_d^V\right)\cdot\mathbf{n} = \beta_C\left(\rho_V - \rho_V^{\infty}\right) \qquad on\ \ \Gamma_C^q \tag{11}$$

where h_T(W/(m^2·K)) denotes the heat exchange coefficient of concrete, including both convection and radiation effects[27]; β_C(m/h) represents the humidity exchange coefficient between the interior and exterior of the concrete, which is dependent on air pressure, temperature, concrete surface heat release coefficient, and other variables[34]; T_{∞} (K) and ρ_V^{∞} (kg/m^3) are the

temperature and water vapor density in external atmosphere.

2.2 Transport and consumption of oxygen

The transport of oxygen through the concrete cover to the steel surface is governed by Fick's law. The diffusion coefficient of oxygen in concrete, D_{O_2}(m^2/s), is determined by the material properties of concrete, temperature and humidity[35]:

$$D_{O_2} = 1.92\times10^{-6}\times\phi_{cp}^{\ 1.8}\times(1-H)^{2.2}\times\exp\left\{\frac{\Delta U_D}{R}\left[\frac{1}{T_0}-\frac{1}{T}\right]\right\} \tag{12}$$

where ϕ_{cp} represents the porosity of the cement paste[36]; T_0=25℃ is the reference temperature; ΔU_D(kJ/mol) represents the activation energy of oxygen diffusion[20]. The concentration of dissolved oxygen on the surface of the concrete cover declines with an increase in temperature[37]:

$$\ln(C_{O_2}^S) = -139.344+\frac{1.575\times10^5}{T}-\frac{6.642\times10^7}{T^2}+\frac{1.244\times10^{10}}{T^3}-\frac{8.622\times10^{11}}{T^4} \tag{13}$$

where $C_{O_2}^S$(mg/liter) represents the concentration of dissolved oxygen in concrete pore solution.

Steel corrosion involves a series of electrochemical reactions, primarily the oxidation of iron and the consumption of oxygen from the surrounding micro-environment of the steel rebars. When the oxygen supply from the external atmosphere matches the oxygen consumed by cathodic reactions, the relationship between the oxygen concentration at the steel-concrete interface and the corrosion current density is[38]:

$$\frac{i_{O_2}}{4F} = -\mathbf{n}\cdot\left(D_{O_2}\nabla C_{O_2}\right)\Big|_{interface} \tag{14}$$

where i_{O_2} (A/m^2) represents the cathodic current density at the steel-concrete interface; F=96485(C/mol) is Faraday constant; **n** is the unit normal vector. This equilibrium is not only influenced by the transport and consumption process of oxygen, but also by its solubility equilibrium.

Gaseous oxygen diffuses from the external environment through the concrete pores to the steel surface, where dissolved oxygen participates in the cathodic reaction of the corrosion process. Gaseous oxygen and dissolved oxygen interconvert, leading to changes in the oxygen concentration available for the corrosion process, and this process is influenced by environmental

temperature. The gaseous oxygen concentration $\rho_{O_2}^{gas}$ (kg/m^3) and the dissolved oxygen concentration $\rho_{O_2}^{liq}$(kg/m^3) are in a state of solubility equilibrium described by Henry's law[21]:

$$\rho_{O_2}^{liq} = \frac{RTn_{H_2O}}{H_{O_2}} \cdot \rho_{O_2}^{gas} \tag{15}$$

where H_{O_2}(Pa) is the Henry's constant of oxygen, which depends on temperature; n_{H_2O} is the molar number of water in a dilute solution of a cubic meter.

2.3 Transport of chloride ions

Chloride ions destroy the passive film on the steel surface, causing the steel to lose protection and thus initiating corrosion reactions. Chloride ions serve as catalysts that accelerate the transition of rebar from a passive to an activated state. The concentration of chloride ions on the steel surface determines the locations of anodic and cathodic areas. This, in turn, controls the non-uniform corrosion rate and influences the shape of the corroded cross-section. Reinforced concrete structures experience dry-wet cycles under marine environments, leaving the structures in an unsaturated state. Ababneh proposed a partial differential equation to characterize the transport of chloride ions in unsaturated concrete[39]:

$$\frac{\partial C_{Cl}^{fr}}{\partial t} = \frac{\partial C_{Cl}^{fr}}{\partial C_{Cl}^{to}} \left(\nabla \left[D_{Cl} \nabla (C_{Cl}^{fr}) \right] + \nabla \left[D_{wt} \frac{\rho_{con}}{\phi S \rho_{sol}} C_{Cl}^{fr} \nabla (H) \right] \right) \tag{16}$$

where C_{Cl}^{fr} and C_{Cl}^{to} denote the free and total chloride ions content (wt.% of concrete), with the Langmuir binding model describing the relationship between them[40]; D_{Cl} and D_{wt} are the diffusion coefficients of chloride ions and moisture in concrete (m^2/s)[41]; ρ_{con} and ρ_{sol} represent the densities of concrete and environmental chloride solution (kg/m^3); S is the pore saturation of concrete.

The chloride ions diffusion coefficient is determined by both the concrete's microstructural features and environmental factors[42]. The chloride ions diffusion coefficient at any location in the concrete is:

$$D_{Cl}(t) = D_{Cl}^{ref} \times F_{Cl}(T) \times F_{Cl}(H) \tag{17}$$

where $F_{Cl}(T)$ represents the temperature influence coefficient on chloride diffusion, derived from Arrhenius's law[20]; $F_{Cl}(H)$ represents the humidity influence coefficient on chloride diffusion,

which is related to the critical humidity H_C[43]; D_{Cl}^{ref} (m^2/s) represents the effective diffusion coefficient of chloride ions, which characterizes the transport performance under ideal environmental conditions[42]. The details of chloride ions transport under time-varying environment are available in the authors' previous studies[15, 44, 45].

2.4 Electrochemical polarization of steel corrosion

The steel corrosion process follows the law of conservation of charge, i.e., the Laplace equation[46]:

$$\nabla \cdot \mathbf{i} = \nabla \cdot \left(\frac{1}{\rho_c} \nabla \phi \right) = 0 \tag{18}$$

where $\mathbf{i}$(A/m^2) is current flow in concrete; ϕ(V) denotes the potential distribution at the steel-concrete interface; ρ_c(Ω·m) is the resistivity of concrete characterized by a probabilistic prediction model[47].

When modeling steel corrosion, it is essential to account for the electrochemical polarization processes in macrocell and microcell corrosion. Macrocell corrosion and microcell corrosion are two common forms of electrochemical corrosion in reinforced concrete structures, both of which involve anodic and cathodic reactions. Chloride ions governs the activation polarization of steel, thereby playing a crucial role in initiating corrosion[48]. Oxygen supply impacts cathodic polarization and is vital during the corrosion propagation phase[9]. Concrete resistivity significantly affects the circulation of macrocell currents between anodes and cathodes[15]. To describe how these three factors influence the whole corrosion process, the electrochemical polarization theory is introduced. In this paper, Tafel polarization curves and the Butler-Volmer equations are utilized to describe the relationship between anode and cathode potentials and current densities, with the cathodic limiting current density introduced to characterize the polarization behavior of the cathodic reaction[9]. Therefore, the electrochemical polarization of macrocell and microcell is:

$$i_{mac}^{a} = i_{Fe}^{0} \exp\left(2.303 \frac{\phi - \phi_{Fe}^{0}}{\beta_{Fe}} \right) - \frac{i_{O_2}^{0} \exp\left(2.303 \dfrac{\phi - \phi_{O_2}^{0}}{\beta_{O_2}} \right)}{1 + \dfrac{i_{O_2}^{0}}{i_L} \exp\left(2.303 \dfrac{\phi - \phi_{O_2}^{0}}{\beta_{O_2}} \right)} \tag{19}$$

$$i_{mac}^{p} = -\frac{i_{O_2}^{0}\exp\left(2.303\frac{\phi-\phi_{O_2}^{0}}{\beta_{O_2}}\right)}{1+\frac{i_{O_2}^{0}}{i_L}\exp\left(2.303\frac{\phi-\phi_{O_2}^{0}}{\beta_{O_2}}\right)} \tag{20}$$

$$i_{mic}^{a} = \frac{i_{O_2}^{0}\exp\left(2.303\frac{\phi-\phi_{O_2}^{0}}{\beta_{O_2}}\right)}{1+\frac{i_{O_2}^{0}}{i_L}\exp\left(2.303\frac{\phi-\phi_{O_2}^{0}}{\beta_{O_2}}\right)} \tag{21}$$

where i_{mac}^{a} and i_{mac}^{p} are the macrocell corrosion current densities in active and passive regions; i_{mic}^{a} is the microcell corrosion current density in active region; i_L(A/m^2) is the cathodic limiting current density; i_{Fe}^{0}, $i_{O_2}^{0}$, ϕ_{Fe}^{0}, $\phi_{O_2}^{0}$, β_{Fe} and β_{O_2} are key electrochemical parameters[9]. Specific technical details about the electrochemical polarization of steel corrosion can be found in the authors' previous studies[45, 49].

3. Accelerated corrosion test of steel in time-varying environment

3.1 Manufacturing process of specimens

Both mortar and concrete specimens were poured with a water-cement ratio of 0.53, with each cubic meter of mortar containing 538 kg of Portland cement, 285 kg of water, and 1076 kg of fine aggregate, while each cubic meter of concrete was composed of 368 kg of Portland cement, 195 kg of water, 735 kg of fine aggregate, and 1103 kg of coarse aggregate. PI 42.5 standard Portland cement served as the binder, with natural river sand (fineness modulus: 2.11) acting as fine aggregate and 5~10 mm continuously graded gravel designated as coarse aggregate. Tap water was utilized for mixing, and HPB300 steel rebar with a diameter of 10mm was applied. Steel bars were used after removing oxide scales by sandpaper grinding.

Three types of specimens were prepared, namely A, B, and C. Specimen A measured 150×150×300 mm³ and consisted of one mortar and one concrete specimen, each equipped with four oxygen concentration sensors and four temperature and humidity sensors. Specimen B, also sized at 150×150×300 mm³, included one mortar and one concrete specimen, with eight embedded steel rebars for testing corrosion current density. Specimens C measured 150×150×150 mm³ and consisted of four mortar and four concrete specimens, without any embedded steel rebar or

sensors, to examine the distribution of chloride ions concentration under identical exposure conditions. Naming rules for the specimens are illustrated in **Fig. 1**.[36] After pouring, all specimens were cured at 20°C and 95% humidity for 28 days.

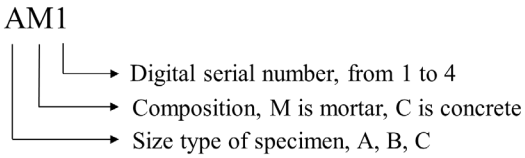

Fig. 1 Specimen naming guidelines[36]

3.2 Methods for detecting medium transport and steel corrosion rate

Each type A specimen contained four temperature-humidity sensors: two positioned at a depth of 1cm and two at 3cm, as illustrated in **Fig. 2**. Additionally, four oxygen sensors were embedded in the same specimens, with the same depth distribution of two at 1cm and two at 3cm.

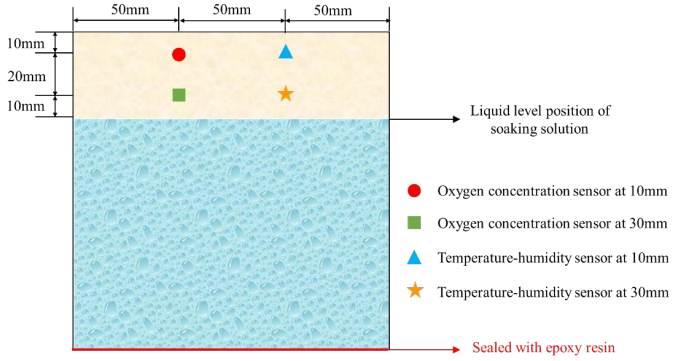

(a)

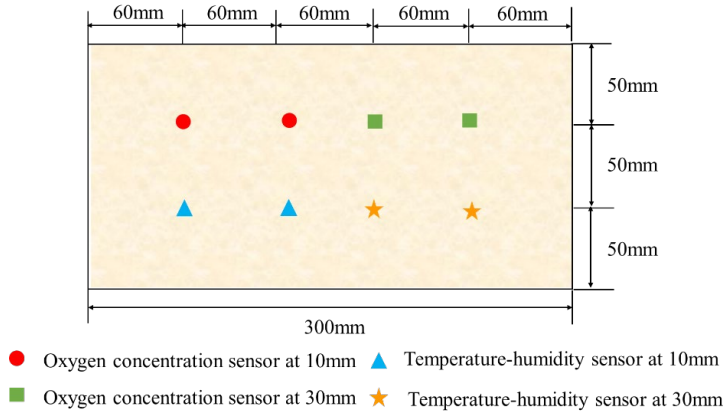

(b)

Fig. 2 Distribution of sensors in specimen A: (a) Side view, (b) Top view.

To simulate a variety of environmental conditions within the same specimen, each type B

specimen was arranged with eight steel rebars, as shown in **Fig. 3**. These rebars were organized into two rows, with four rebars in each row. The upper row had a concrete cover thickness of 10 mm, positioning it closer to the external atmosphere, while the lower row was near the liquid level of the soaking solution, placing it in a high-humidity area. In this study, the heterogeneity of concrete materials was not considered, resulting in symmetrical environmental conditions for steel rebars M and M', as well as for steel rebars N, P, and Q.

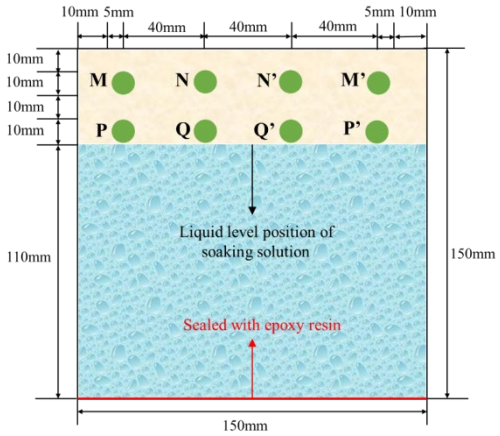

Fig. 3 Arrangement of steel rebars in specimen B

Fig. 4 shows the layout of chloride ions concentration test points. Each sample has three intermediate and three edge test points, 75 mm and 25 mm from the edge, respectively.

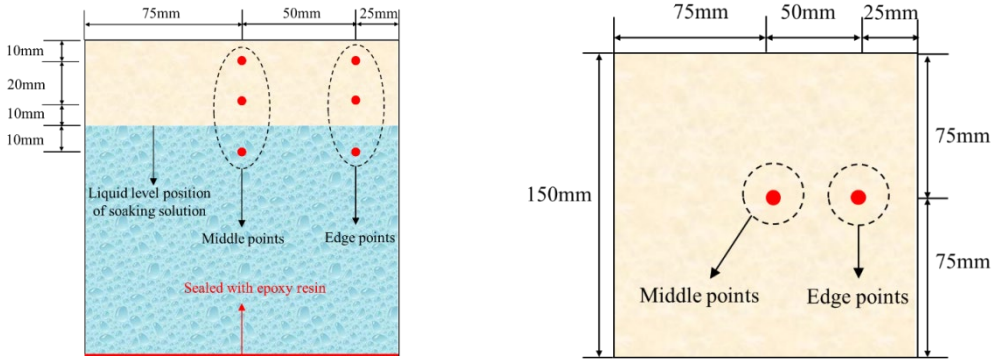

(a) **(b)**

Fig. 4 Layout of chloride ions concentration test points in specimen C: (a) Side view, (b) Top view.

As illustrated in **Fig. 5**, JWSK-6ACC05D temperature-humidity sensors were embedded in type A specimens to monitor the distribution of heat and moisture in concrete. Before pouring, a cylindrical cork covered with waterproof tape was inserted into a PVC pipe having an inner

diameter of 11 mm. These assemblies were then embedded at depths of 10 mm and 30 mm. After curing, the cork was removed, and the sensor probe, encased in sandwich rubber, was inserted into the bottom of the PVC channel. Epoxy resin was applied at contact points for sealing. Temperature and humidity data were recorded hourly.

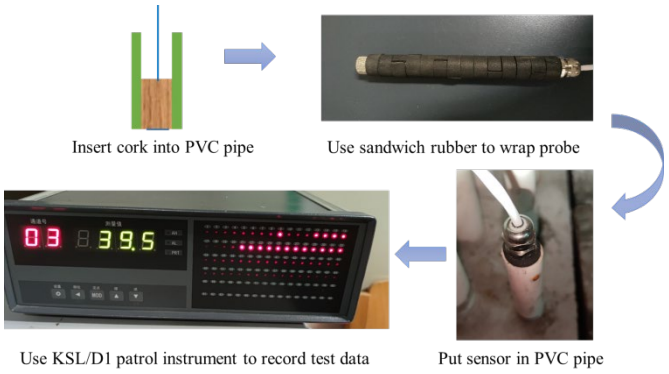

Fig. 5 Embedding process of temperature-humidity sensors

KY-2F oxygen sensors were embedded in type A specimens to measure oxygen at various depths, following the same installation method as temperature-humidity sensors. The test value of oxygen concentration was recorded every 4 days. **Fig. 6** presents the layout of different sensors in specimen A. The sensor layout is adapted from the experimental framework established in the authors' previous research[36].

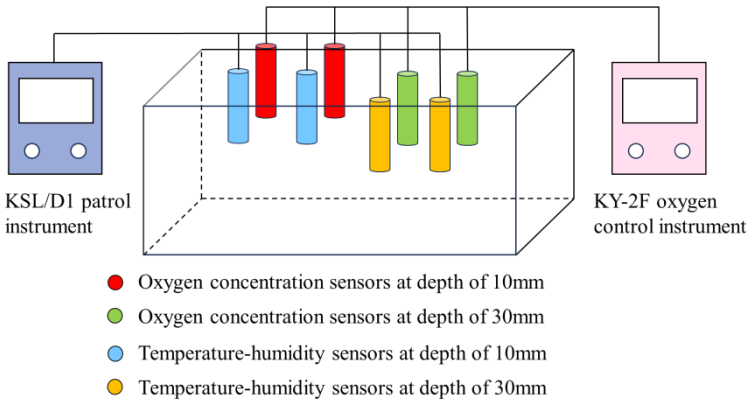

Fig. 6 Layout of various sensors in specimen A[36]

To assess chloride ions distribution, type C specimens were prepared and exposed under the same exposure conditions with type A and B specimens. BEGILD 6026-2 drilling machine was used to locate the concrete surface, and a cylindrical core with a length of 5cm was taken. It is necessary to keep the specimen dry to prevent moisture convection from affecting the test results of chloride ions. The cores were ground with an HDM-150 grinder, reducing speed near the

target depth to prevent damage. The powder was further ground, sieved (0.16 mm), and 4 g dissolved in 40 g deionized water. After 24 hours, free chloride ions content was measured using a DY2501-B analyzer, averaging three tests per point. The test process of chloride ions concentration and the sampling strategy follow those described in the authors' previous research[36], as shown in **Fig. 7**.

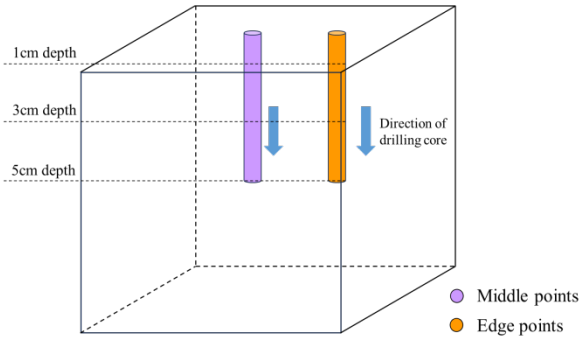

Fig. 7 Layout of sampling points for chlorine test[36]

Linear polarization method was used to test the corrosion current density in specimen B, which was described in detail in the authors' previous research[36]. Steel rebars were polished with sandpaper, and then the wires were welded on the exposed steel matrix. Each steel rebar was welded with one wire. Waterproof tape was used to wrap the connection between wire and steel. The part of steel rebar exposed to the outside of concrete was covered with a PVC pipe, and kaft glue and epoxy resin were injected between PVC pipe wall and steel rebar to play a role in sealing protection. CHI660E electrochemical workstation was used in the test. A 30mm×30mm stainless-steel sheet was used as the auxiliary electrode, with a 100mm×100mm wet sponge placed near the measuring point and the reference electrode above the specimen. The concrete was fully saturated to ensure stable contact between the electrode and steel rebar. The polarization potential was 20mV, the scanning rate was 0.166mV/s, and 100~150s were required to achieve a stable corrosion potential.

3.3 Accelerated corrosion process

To simulate steel rebar corrosion in a marine environment, specimens underwent a two-day cyclic temperature and humidity variation to accelerate chloride ions and moisture transport, as shown in **Fig. 8**. As shown in **Fig. 9**, a TEMI880 programmable temperature and humidity chamber with a temperature control accuracy of ±0.5 ℃ and humidity control accuracy of ±2 %

was employed to carry out the simulation. Specimens were submerged in a 5% NaCl solution at a depth of 11 cm for 180 days.

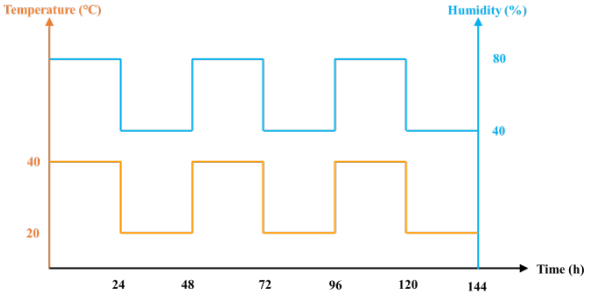

Fig. 8 Temperature and humidity variations in the test chamber

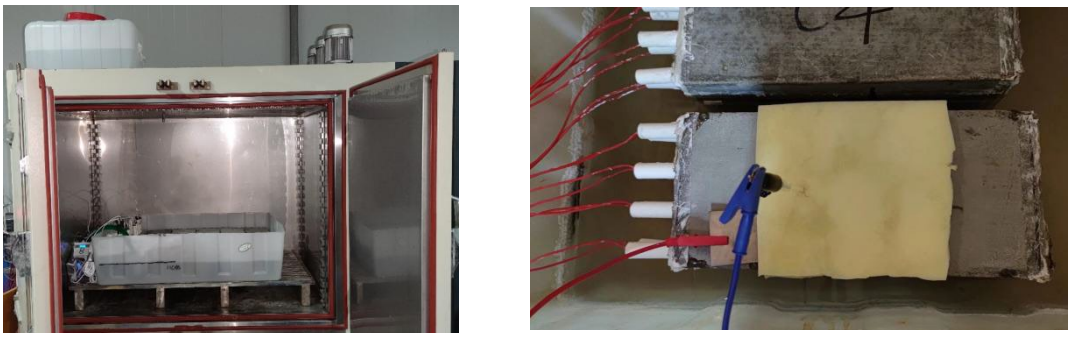

(a) **(b)**

Fig. 9 Accelerated corrosion test under time-varying environment: (a) Exposure of the specimens, (b) Specimens soaked in solution for testing[36].

3.4 Finite element modeling and parameter selection

The model parameters used in this study are summarized in **Table 1**. Due to differences in material composition, the transport rates of mortar and concrete vary. Notably, the chloride ions diffusion coefficient is not constant, as it is influenced by temperature and humidity fluctuations. **Table 1** provides reference values for the diffusion coefficient, while the actual chloride ions transport rate is calculated using Eq. (17). Similarly, the oxygen diffusion coefficient and surface oxygen concentration are also affected by temperature and humidity in the time-varying environment. Additionally, the heat and moisture exchange coefficients of concrete were treated as time-dependent variables influenced by environmental temperature and humidity. In addition, the electrochemical parameters adopted in this study are consistent with those reported in the authors' previous research[36].

Table 1 Corrosion parameters of mortar and concrete models

Parameters	Value	Source
Concrete cover thickness C (mm)	10	Test condition
Steel rebar diameter D (mm)	10	Test condition
Dimensions of concrete section L×W (mm^2)	150×150	Test condition
Water-binder ratio *w/c* (-)	0.53	Test condition
Environment temperature T_{en} (K)	293~313	Test condition
Environment humidity H_{en} (%)	40~80	Test condition
Reference diffusion coefficient of chloride ions D_{cl}^{ref} (m^2/s)	12×10^{-12} for mortar, 5×10^{-12} for concrete	Reference[42]
Chloride ions concentration on concrete surface C_{Cl}^{S} (wt.% of concrete)	0.677	Test condition
Initial chloride ions concentration C_{Cl}^{0} (wt.% of concrete)	0	Test condition
Critical chloride concentration C_{Cl}^{crit}(wt.% of cement)	0.4	Reference[50]

The finite element simulation was performed using COMSOL Multiphysics®, as shown in **Fig. 10**. In order to enhance the calculation accuracy, a boundary layer was applied at the steel-concrete interface. During the meshing process, eight iterations were carried out, and the maximum depth of each element was set to eight. The mesh size ranged from 0.0025 cm to 0.74 cm. The chloride ions concentration on the concrete surface exposed to the solution was equated to that in the solution. Inward oxygen diffusion occurred only at atmospheric-exposed boundaries, while there was no oxygen diffusion at boundaries submerged in the solution or sealed with epoxy resin.

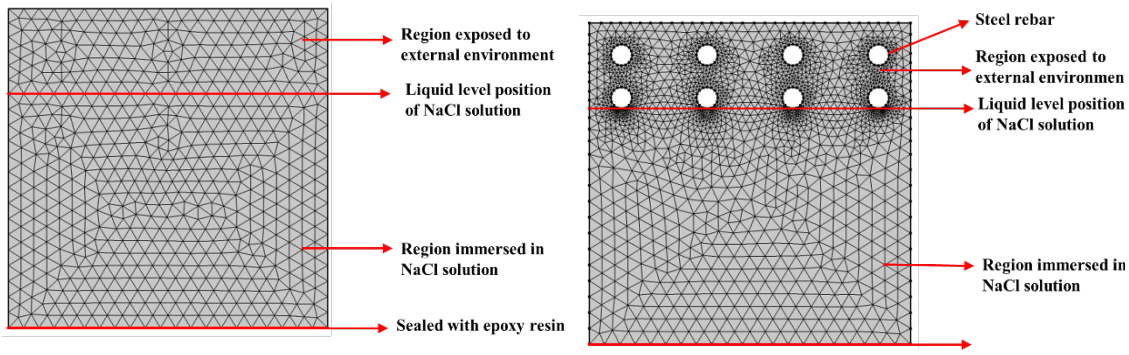

(a) **(b)**

Fig. 10 Meshing of finite element models for various specimens: (a) Specimen A and C[36], (b) Specimen B[36].

4. Model verification results and parameter discussions

4.1 Model verification results

4.1.1 Oxygen concentration

Under the experimental conditions, periodic fluctuations in temperature and humidity caused corresponding variations in surface oxygen concentration and oxygen diffusion coefficients. Consequently, the oxygen concentration within the specimens also exhibited periodic fluctuations, as illustrated in **Fig. 11**. The oxygen concentration fluctuations at a depth of 1 cm are consistently greater than those at 3 cm for both mortar and concrete specimens. This behavior is attributed to the non-uniform humidity distribution within the specimens. Measuring points closer to the exposed surface are more influenced by external humidity fluctuations, leading to more pronounced changes in humidity[45]. According to the simulation results, the minimum oxygen concentration at both depths is identical, approximately 0.176 mol/m³. However, the peak oxygen concentration at 1 cm is significantly higher than at 3 cm. This difference stems from the reduced diffusion distance to the external atmosphere at 1 cm.

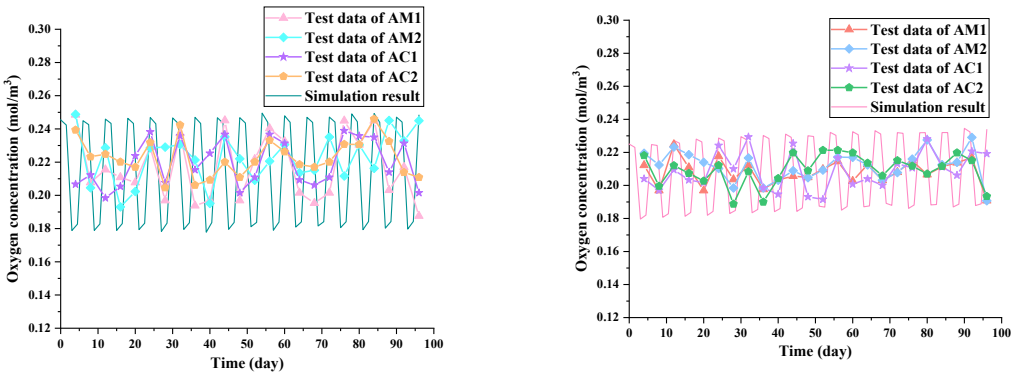

(a) **(b)**

Fig. 11 Comparison of measured and simulated oxygen concentration at different depths in mortar and concrete: (a) 1cm, (b) 3cm.

As shown in **Fig. 12**, the average relative error measures 12.3%. The simulation results show a broader fluctuation range in oxygen concentration when compared with the experimental data. The error mainly stems from the fact that the model does not consider the influence of initial

oxygen content inside the concrete. Additionally, the model predicts greater humidity fluctuations than observed experimentally, contributing to the fluctuation in oxygen concentration. Considering the complex mechanisms involved in the model, the simulation results are highly sensitive to external environmental changes. Overall, the experimental data show good agreement with the model predictions.

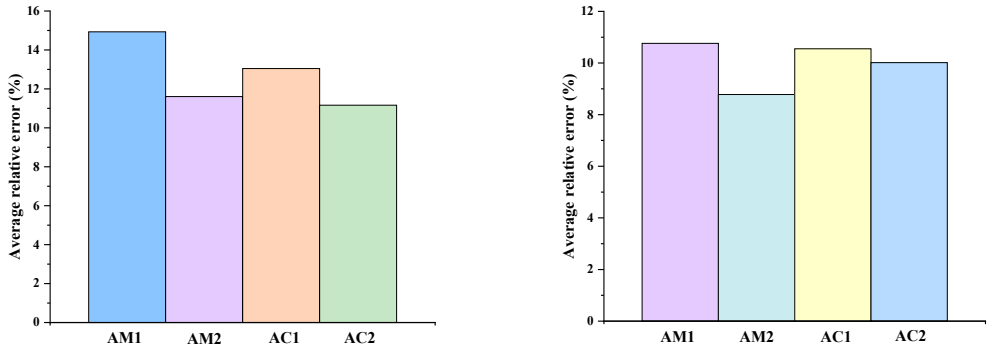

Fig. 12 Relative error of oxygen concentration at two different depths (%): (a) 1cm, (b) 3cm.

4.1.2 Temperature

As shown in **Fig. 13**, the temperature distribution within mortar and concrete specimens is relatively uniform across different depths. The temperature range for mortar is 20°C to 40.1°C, for concrete is 20°C to 40.7°C, while simulation results range from 20°C to 40°C. Experimental data generally show higher temperatures than simulations at 20°C and lower temperatures at 40°C, reflecting smaller variations in internal temperature compared to the external environment. Despite these differences, the experimental data align well with the simulation results overall.

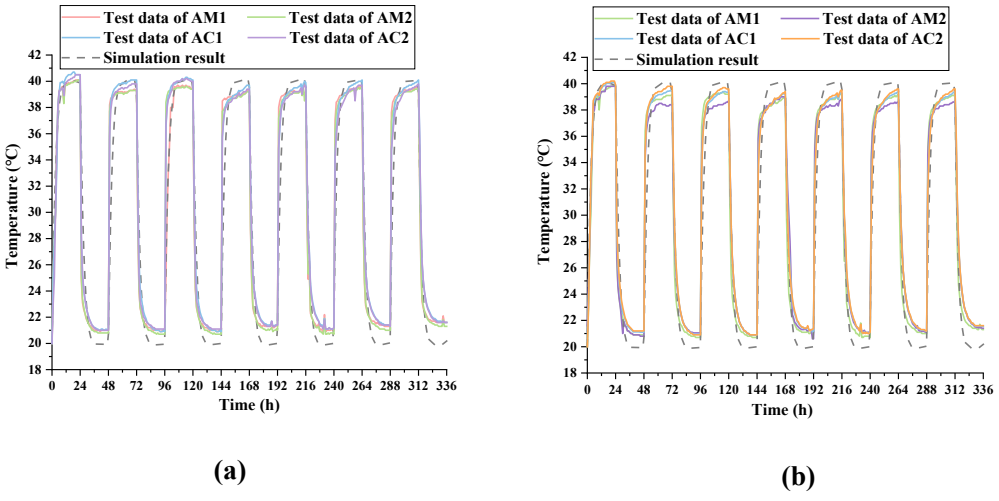

Fig. 13 Comparison of measured and simulated temperature results: (a) 1cm depth, (b) 3cm

depth.

4.1.3 Relative humidity

Fig. 14 presents a comparison between experimental humidity data and simulation results. In both mortar and concrete specimens, humidity fluctuations at 3 cm depth are less pronounced than at 1 cm, as the 1 cm layer is more strongly influenced by external environmental humidity. At 3 cm, closer to the soaking solution, humidity maintains a consistent high level of around 95%, indicating a non-uniform moisture distribution within the specimens.

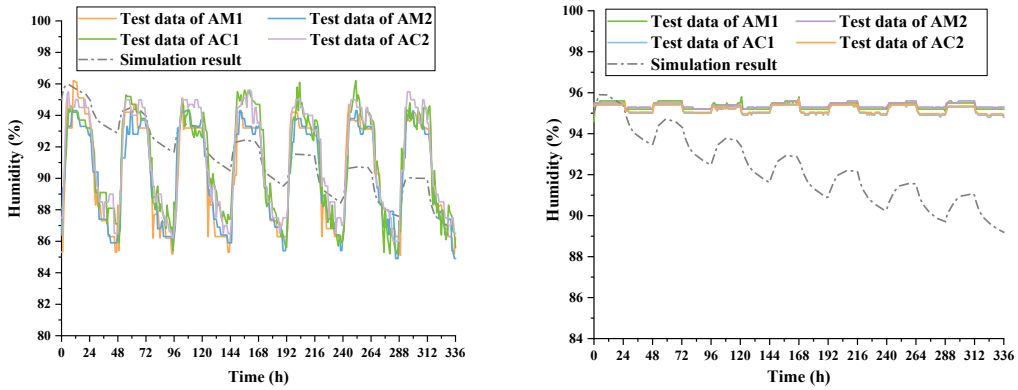

Fig. 14 Comparison of measured and simulated humidity results: (a) 1cm depth, (b) 3cm depth.

The simulation results show a downward trend in humidity, while the test data remain nearly unchanged across different cycle periods. This difference is due to the initial humidity setting in the modelling. At the start of exposure, the humidity inside the concrete is non-uniform, but the numerical model assumes a fixed initial humidity, resulting in inaccuracies in the initial distribution. In actual experiments, the moisture exchange coefficient of the concrete surface layer is relatively small, while that of the inner part is relatively large, a significant difference that has not been reflected in the simulation process. The holes where the sensor probes are placed were reserved during the pouring process of the specimens. So, there may be an enrichment of moisture on the interface around the humidity sensor probe, which leads to the concentration of humidity, resulting in the test data of humidity higher than the simulation result. These lead to errors in the simulation results of humidity. Overall, the simulation results of humidity align well with the experimental data.

4.1.4 Chloride ions concentration

Fig. 15 presents a comparison between experimental data and simulation results of chloride ions concentration. Chloride ions concentration exhibits a decreasing trend as vertical depth increases. Among the six testing points, the peak chloride ions concentration is 0.333% for mortar and 0.226% for concrete, with both maxima occurring at a 1 cm depth near the edge exposed to the atmosphere. The top 4 cm of the specimen undergoes periodic dry-wet cycles, leading to frequent humidity fluctuations. This promotes chloride ions convection as the main transport mechanism, resulting in noticeable chloride ions accumulation in this region. At the same vertical depth, chloride ions concentration at the edge consistently exceeds that in the middle region, due to the edge's proximity to the soaking solution.

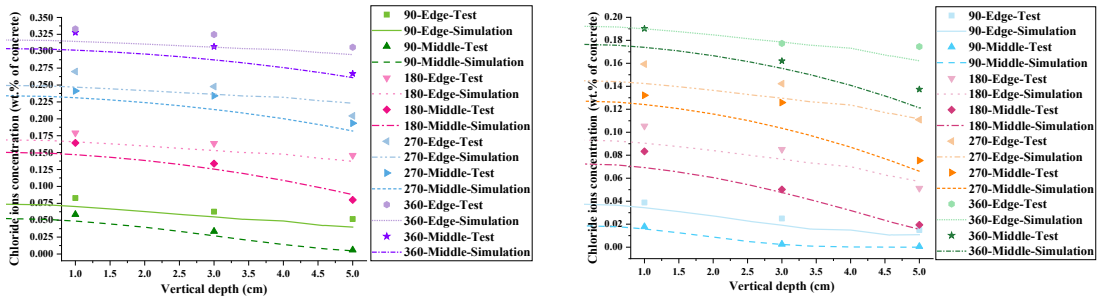

(a) **(b)**

Fig. 15 Comparison of measured and simulated chloride ions concentration (Data labeling: time(days) - test point location (middle/edge) - data type (test/simulation)): (a) Mortar, (b) Concrete.

The higher porosity of mortar results in a larger chloride ions diffusion coefficient compared to concrete. Therefore, at the same testing point and time, chloride ions concentration in mortar is consistently higher than that in concrete. Notably, the simulation results for mortar show closer alignment with the experimental data. This is likely attributed to the model's assumption that both mortar and concrete are homogeneous materials, which overlooks the heterogeneity induced by coarse aggregates in concrete structures. Overall, the chloride ions concentration data for both mortar and concrete exhibit good consistency with the simulation results.

4.1.5 Corrosion current density

Figs. 16 and **17** reveal a marked decreasing tendency in the current densities of steel rebars, suggesting that macrocell corrosion is the dominant form of steel corrosion[45]. As time

progresses, the active region on the rebar surface enlarges, leading to a gradual reduction in macrocell corrosion. The experimentally measured corrosion current density is slightly higher than the simulation results, attributed to the two-dimensional model, which accounts for circumferential corrosion but overlooks longitudinal corrosion. Additionally, in actual tests, boundary effects and epoxy resin sealing effectiveness result in more significant corrosion at the sealed ends of rebars. Despite these discrepancies, the experimental and simulation outcomes exhibit consistent trends, validating the model's efficacy in simulating the evolution of steel corrosion rate.

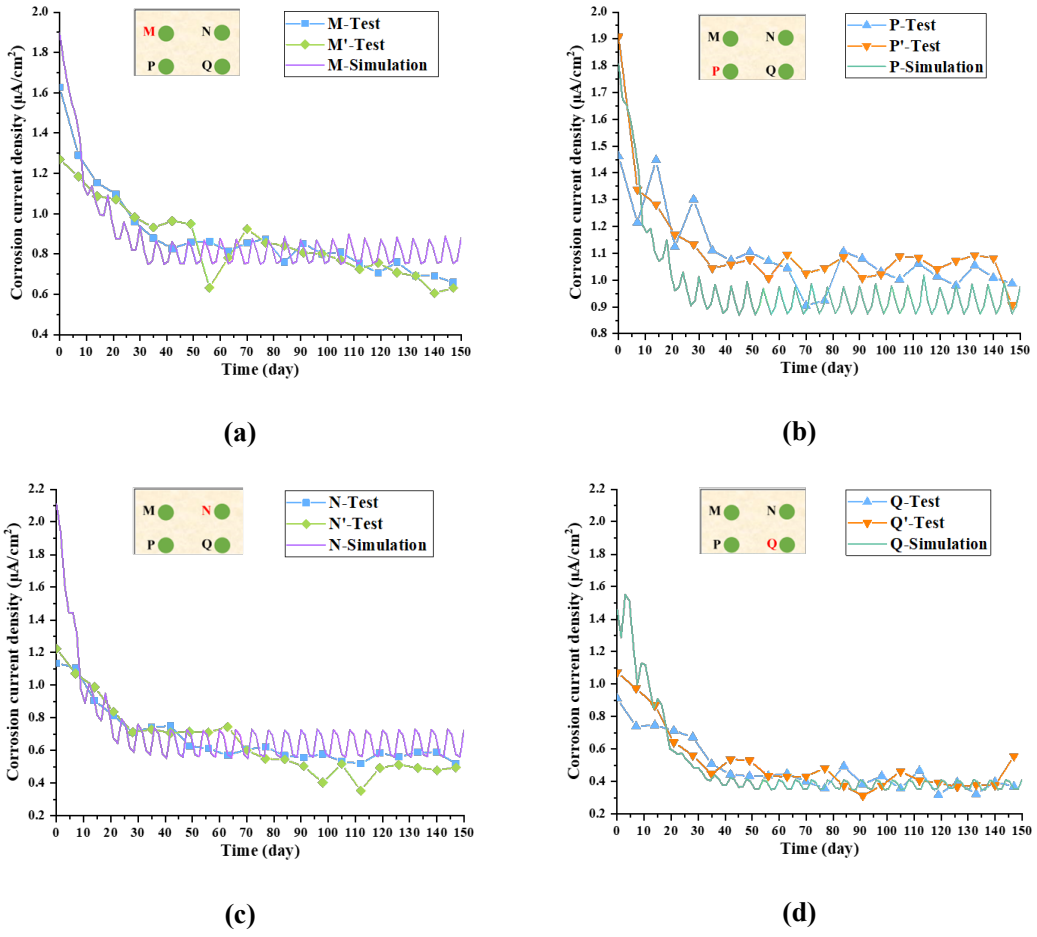

Fig. 16 Comparison of measured and simulated corrosion current densities in mortar: (a) Rebar M, (b) Rebar P, (c) Rebar N, (d) Rebar Q.

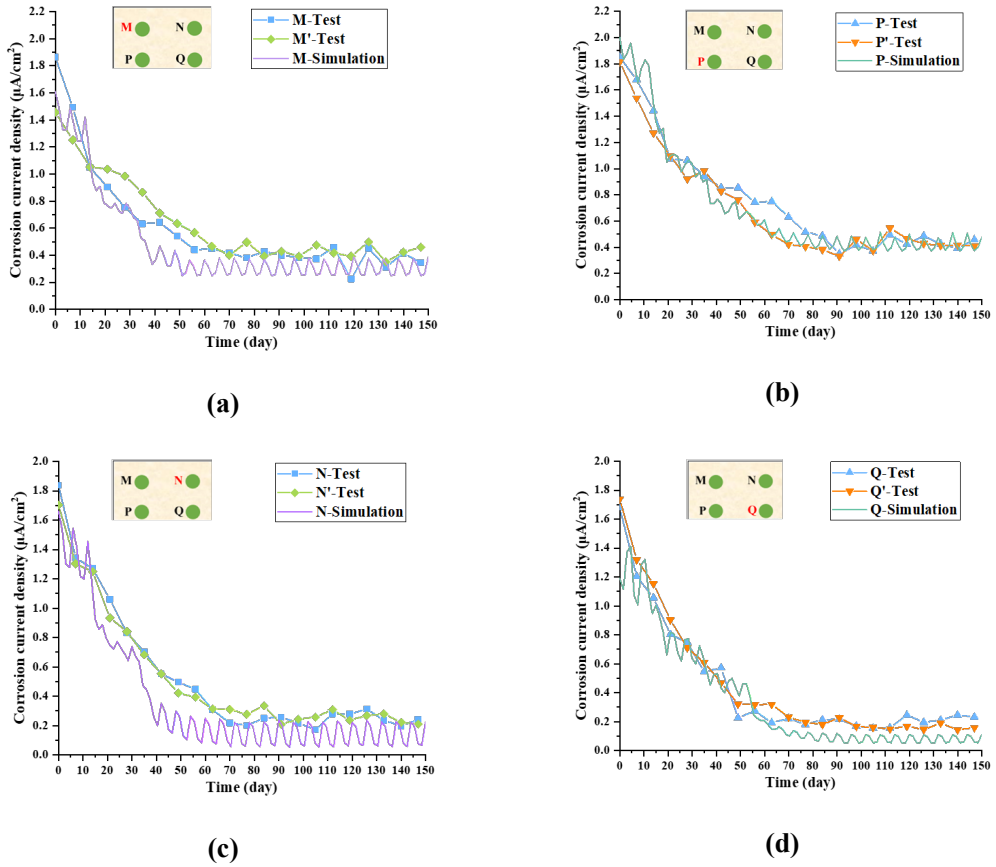

Fig. 17 Comparison of measured and simulated corrosion current densities in concrete: (a) Rebar M, (b) Rebar P, (c) Rebar N, (d) Rebar Q.

Both experimental and simulation results demonstrate the corrosion current density of rebar P is slightly higher than that of rebar M. This phenomenon is primarily attributed to rebar P's proximity to the NaCl solution, which leads to a higher chloride ion concentration on its surface and earlier activation. The increased chloride ions concentration reduces the resistivity of concrete, further contributing to the increased corrosion current density. In comparison to the other three rebars, rebar Q, being the farthest from the external environment, exhibits the least sensitivity to temperature and humidity fluctuations, resulting in minimal variations in current density.

4.2 Parameter discussions

4.2.1 Distribution of oxygen concentration in concrete

The cathodic reaction of corrosion significantly affects oxygen concentration distribution in concrete. Despite identical exposure conditions, specimens A and B in **Fig. 18** exhibit distinct oxygen concentration profiles. In specimen A, without steel rebars, oxygen distribution is governed solely by transport processes, without consumption effects. The upper 4 cm of specimen

A, located in the atmospheric zone, shows high oxygen concentration, while the lower 11 cm in the immersion zone has low levels. In specimen B, the oxygen concentration is higher on the upper surface of the first-row steel rebar due to its proximity to the external atmosphere. The second-row rebars in specimen B, being closer to the solution surface and exposed to higher chloride ions concentration, undergo corrosion earlier, resulting in significantly lower oxygen concentration compared to surrounding areas.

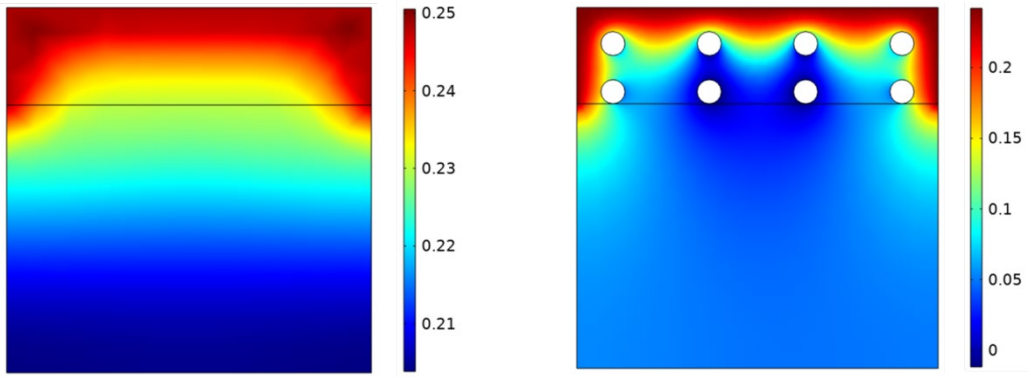

Fig. 18 Simulated oxygen concentration distribution in concrete on day 150 (mol/m^3): (a) Specimen A, (b) Specimen B.

As shown in **Fig. 19**, rebars M and P display higher oxygen concentrations on their left sides, as these sides are closer to the external atmosphere, reducing the diffusion distance and enhancing oxygen flux. Additionally, oxygen concentration is notably higher at 270° compared to 90°, as the region near 270° is closest to the soaking solution. This proximity results in higher chloride ions concentrations, activating this area as the anode in corrosion cells. Other regions on the rebar surface with lower chloride ions concentrations act as cathodes, consuming more oxygen and thereby showing lower concentrations.

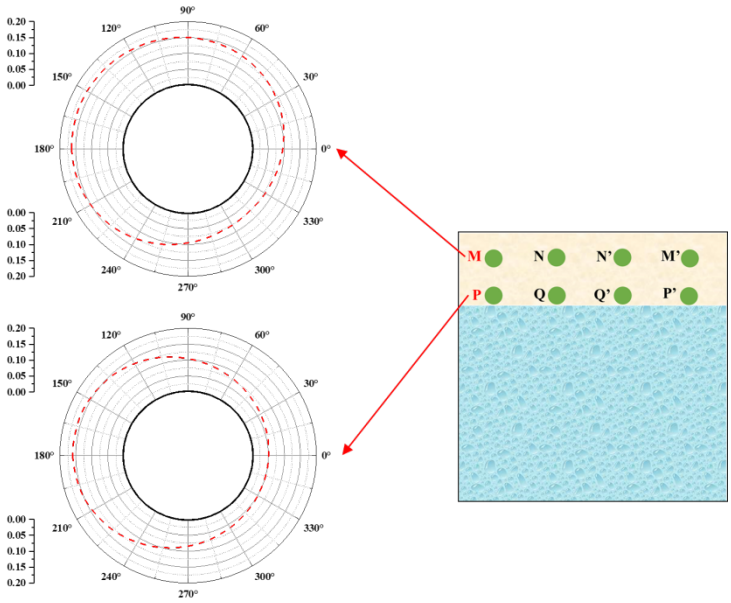

Fig. 19 Simulated oxygen concentration distribution on steel M and P surfaces at day 150 (mol/m^3)

4.2.2 Effect of temperature on oxygen concentration

The effect of temperature on oxygen concentration in specimen A is shown in **Fig. 20**. Initially, oxygen concentration is low but increases over time as oxygen diffuses into the concrete. Temperature fluctuations cause periodic changes in both temperature and oxygen concentration, with a negative correlation between them. Without steel reinforcement in specimen A, oxygen concentration depends only on diffusion. Higher temperatures accelerate diffusion but reduce dissolved oxygen concentration and solubility, with the latter effect dominating. In reinforced concrete, temperature also impacts oxygen consumption by accelerating chloride ions diffusion, reducing resistivity, and increasing reaction rates.

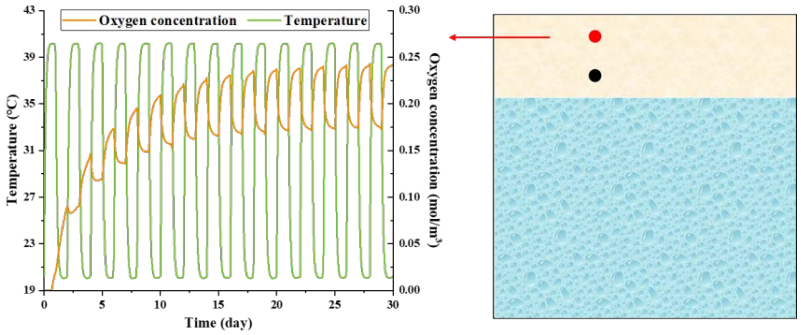

(a)

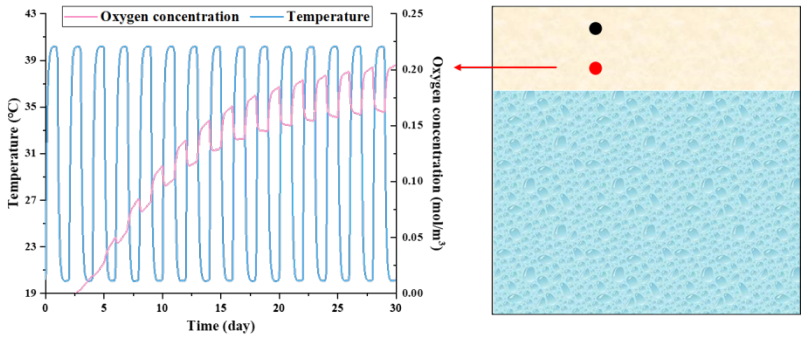

(b)

Fig. 20 Effect of temperature on oxygen concentration at different depths in specimen A (simulation results): (a) 1cm, (b) 3cm.

4.2.3 Effect of humidity on oxygen concentration

Fig. 21 shows significant non-uniform humidity distribution in specimens A and B. The 48-hour cyclic variation in external temperature and humidity results in notable differences between the humidities on days 150 and 151. On day 150, the environment humidity is 80 %. Therefore, the humidity at the boundaries between the two specimens and the external atmosphere is 85%. On day 151, the environment humidity is 40%. Therefore, the humidity at the boundaries between the two specimens and the external atmosphere is 40%. The impact of environmental humidity on the specimen's internal humidity distribution is limited, with the lower part immersed in solution consistently maintaining humidity above 90%. Therefore, the upper 4cm height region of the specimens undergoes frequent dry-wet cycles, while the lower 11cm height region of the specimens is always in a high humidity environment.

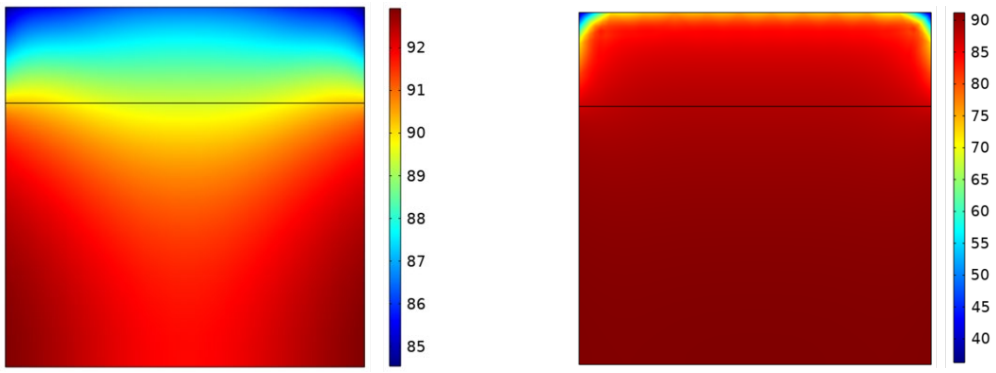

(a) **(b)**

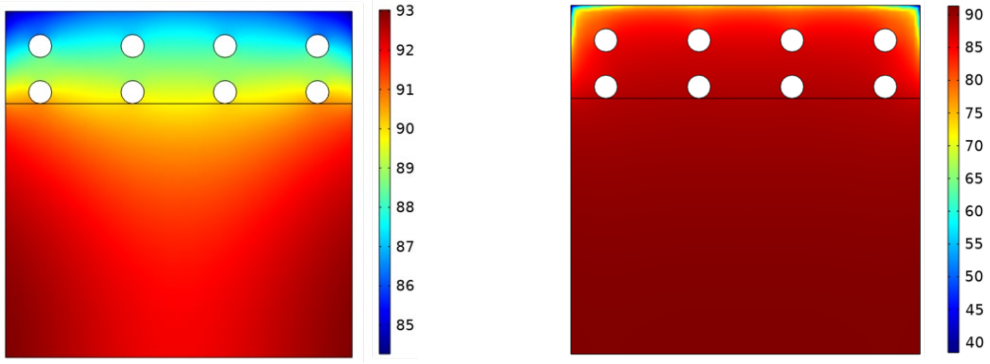

(c) **(d)**

Fig. 21 Simulation results of humidity distribution in specimen A and B: (a) Specimen A, day 150, (b) Specimen A, day 151, (c) Specimen B, day 150, (d) Specimen B, day 151.

As shown in **Fig. 22**, simulated humidity in concrete decreases with depth, while oxygen concentration increases. Initially, high internal humidity results in low oxygen levels. During dry-wet cycles, decreasing internal humidity reduces pore saturation, allowing more oxygen to diffuse through the unsaturated pores. According to Eq. (12), higher humidity reduces the oxygen diffusion coefficient. The combined effects of temperature and humidity suggest that, while elevated levels accelerate chloride ions transport and increase the active area on the steel surface, they also reduce oxygen availability at the steel surface due to lower oxygen diffusion. This limitation in oxygen availability may explain the decline in steel corrosion rates when concrete saturation is too high, a phenomenon noted by previous studies[10, 51].

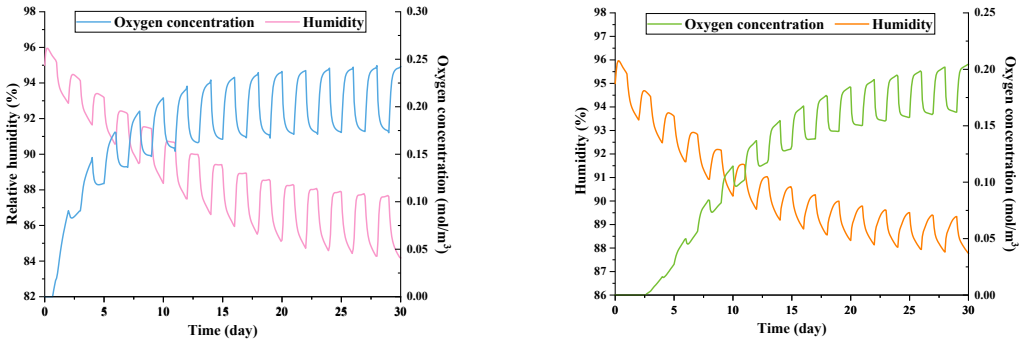

(a) **(b)**

Fig. 22 Effect of humidity on oxygen concentration at different depths in specimen A (simulation results): (a) 1cm, (b) 3cm.

4.2.4 Effect of chloride ions on oxygen concentration

As shown in **Fig. 23**, the lower 11 cm of the specimen, immersed in NaCl solution, has the

highest chloride ions concentration at its boundary. The middle area, farthest from the solution, exhibits the lowest concentration. The upper area of the specimen displays a higher concentration than the middle area. This is due to exposure to the external environment and frequent dry-wet cycles, where moisture convection drives chloride ions to the upper specimen. This pattern differs from that under constant temperature and humidity conditions[15].

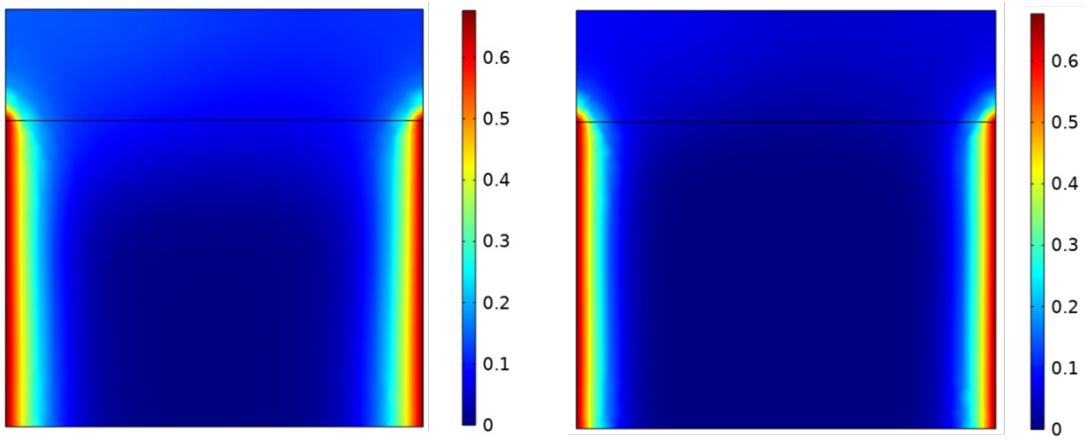

(a) **(b)**

Fig. 23 Simulated chloride ions concentration distribution on day 150 (wt.% of concrete): (a) Mortar, (b) Concrete.

Previous studies have widely recognized that chloride ions and oxygen concentrations were independent variables in the corrosion process[9]. However, as demonstrated in our previous work[36], the chloride ions concentration affects the distribution of anodic and cathodic areas on the steel surface, thereby indirectly influencing oxygen consumption. The present study extends this finding to time-varying environments. As shown in **Fig. 24**, chloride ions concentrations at m and p steadily increase, while oxygen concentration follows a different trend: a sharp rise, a steep drop, and eventual stabilization. Before day 189, the chloride ions concentration at m remains below the critical threshold, keeping the steel surface in a passive state. On day 189, m becomes active, initiating corrosion and causing a significant drop in oxygen concentration. Over time, oxygen diffusion from the atmosphere restores the balance between oxygen inflow and consumption. Furthermore, oxygen concentration shows marked fluctuations, which are more significant than those of chloride ions. This is because chloride ions concentration is mainly controlled by the diffusion process, while oxygen concentration is affected by both diffusion and consumption processes, thus being more sensitive to environmental changes.

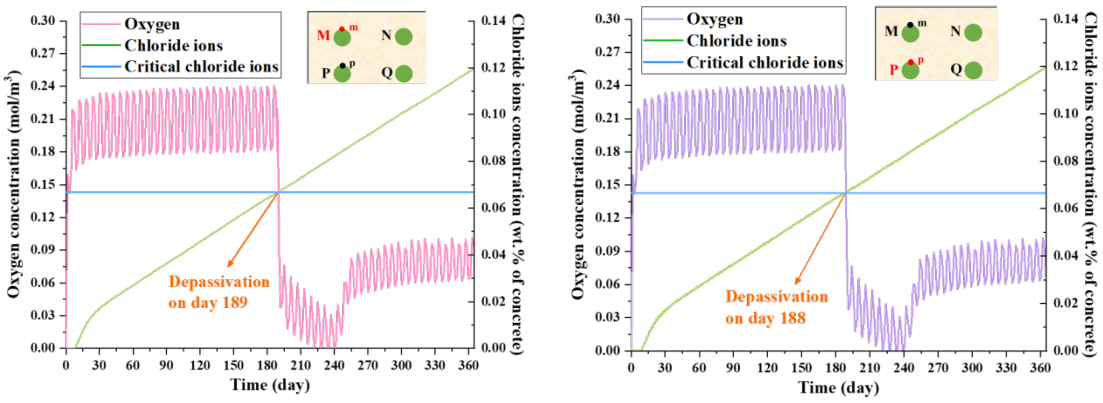

(a) **(b)**

Fig. 24 Relationship between chloride ions concentration and oxygen concentration (simulation results): (a) Point m, (b) Point p.

In conclusion, in the absence of steel, the distribution of chloride ions has a negligible impact on oxygen concentration. When rebars are present, the accumulation of chloride ions leads to rebar depassivation and initiates corrosion. This triggers cathodic oxygen consumption, causing a sharp but temporary decrease in oxygen concentration. Over time, oxygen diffusion from the atmosphere restores balance, establishing a new equilibrium between oxygen diffusion and consumption. However, the final oxygen concentration remains significantly lower than pre-depassivation levels.

4.2.5 Effect of steel corrosion rate on oxygen concentration

As illustrated in **Fig. 25**, prior to the initiation of steel corrosion, higher oxygen concentrations appear near the upper surface of the specimen, while lower concentrations are observed near the bottom surface. Following the initiation of corrosion on day 144, cathodic reactions consume oxygen, leading to a decline in oxygen concentrations on the steel surface.

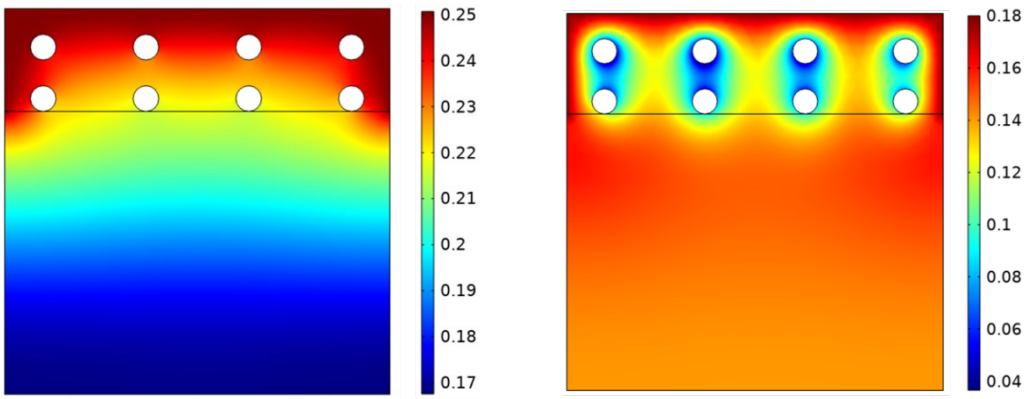

(a) **(b)**

Fig. 25 Simulated oxygen concentration distribution in mortar before and after corrosion (mol/m³): (a) Day 100, non-corroded, (b) Day 145, corroded.

As previously established[36], the onset of corrosion leads to a sharp decline in oxygen concentration on the steel surface. However, under the cyclic temperature and humidity conditions employed in this study, the recovery of oxygen concentration exhibits a distinct pattern compared to that observed under constant environments. Specifically, as shown in **Fig. 26**, following the abrupt drop at depassivation, the oxygen concentration at point m gradually recovers after day 160 owing to the continuous inward diffusion from the external atmosphere, eventually reaching a new equilibrium around day 234 at approximately 0.73 mol/m³. Notably, this recovery process is accompanied by periodic fluctuations in oxygen concentration, which are closely correlated with the cyclic variations in external temperature and humidity. In contrast, under the constant environmental conditions reported in Zhang et al.[36], the oxygen concentration at comparable locations recovered monotonically without such oscillations. Furthermore, the peak corrosion current density at point m occurs slightly after the minimum oxygen concentration, a lag that is attributed to the non-uniform moisture distribution within the specimen, which modulates the concrete resistivity and consequently the intensity of macrocell current circulation. These dynamic features are unique to time-varying exposure conditions and were not captured in previous constant-environment models.

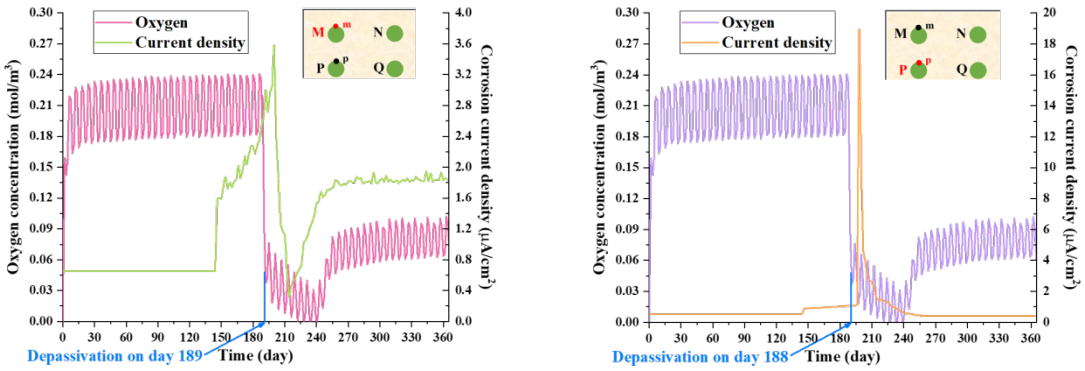

(a) **(b)**

Fig. 26 Relationship between oxygen concentration and corrosion current density at two representative points in mortar (simulation results): (a) Point m, (b) Point p.

5. Conclusions

This study developed a model to describe oxygen availability in the cathode region under varying environmental conditions. The model improved predictions of heat, moisture, chloride, and oxygen transport, as well as corrosion rates. Accelerated corrosion experiments were conducted under dynamic environmental conditions, with real-time monitoring of temperature, humidity, medium concentrations, and corrosion current density in mortar and concrete specimens. The key conclusions were as follows:

(1) Under cyclic temperature and humidity conditions simulating diurnal variations in marine environments, the oxygen concentration within concrete exhibits periodic fluctuations, with greater amplitude occurring near the exposed surface due to more pronounced temperature and humidity variations. In contrast to the relatively stable oxygen distribution observed under constant environments, the time-varying exposure produces a non-uniform and dynamic oxygen field within the concrete cover.

(2) Temperature in concrete is generally uniform, while humidity shows significant variation, influencing oxygen transport. Higher temperatures accelerate oxygen diffusion but reduce oxygen solubility at the concrete surface. Increased humidity lowers oxygen solubility, slowing diffusion rates. Thus, excessively high temperature and humidity can limit oxygen supply to the steel surface, reducing its availability for cathodic reactions.

(3) Under time-varying environmental conditions, steel depassivation triggers a sharp decline in oxygen concentration at the steel surface due to cathodic consumption. However, unlike the monotonic recovery observed under constant environments, the subsequent replenishment of oxygen under cyclic temperature and humidity exhibits periodic fluctuations, eventually stabilizing at a level significantly lower than that prior to depassivation.

(4) A critical time lag is identified between the minimum oxygen concentration and the peak corrosion current density following steel depassivation. This lag, caused by non-uniform moisture distribution modulating concrete resistivity and macrocell current circulation, is a dynamic feature unique to time-varying exposure conditions and cannot be reproduced by models assuming constant environmental parameters.

Acknowledgements

This research is financially supported by Guangdong Provincial Key Laboratory of Intelligent

Disaster Prevention and Emergency Technologies for Urban Lifeline Engineering（2022）（Grant No. 2022B1212010016），National Natural Science Foundation of China (Grant No. 52278223), Zhejiang Provincial Natural Science Foundation of China (LGG22E080003). This research was supported by Zhejiang Provincial Natural Science Foundation of China under Grant No. LQN26E080044.

Author contribution statement

Guo-Yi Zhang is responsible for Conceptualization and Writing – original draft. Ye Tian is responsible for Funding acquisition and Software. Zu-Shi Tian is responsible for Writing – review & editing. Ke-Wei Yu is responsible for Writing - review & editing. All the authors have approved the final manuscript.

Data availability

The data that support the findings of this study is available from the corresponding author upon reasonable request.

Use of AI statement

None.

Declaration of competing interest

The authors have no competing interests to declare that are relevant to the content of this article.

References

[1] Khatami Dena, Hajilar Shahin, Shafei Behrouz (2021) Investigation of oxygen diffusion and corrosion potential in steel-reinforced concrete through a cellular automaton framework. Corrosion Science 187: 109496.https://doi.org/https://doi.org/10.1016/j.corsci.2021.109496

[2] Ding Tiancong, Sun Chong, Sun Jianbo, et al. (2025) A mechanistic model for the corrosion prediction of bare carbon steel in supercritical CO2-H2S-Cl- environments. Corrosion Science 256: 113161.https://doi.org/10.1016/j.corsci.2025.113161

[3] Xiao Zhong, Li Jing, Hou Chen, et al. (2026) Initial corrosion behavior and corrosion-rate modeling of Q355C steel under coupled tensile loading and wet-dry cycling. Corrosion Science 259: 113506.https://doi.org/10.1016/j.corsci.2025.113506

[4] Shafei Behrouz, Alipour Alice (2015) Application of large-scale non-Gaussian stochastic fields for the study of corrosion-induced structural deterioration. Engineering Structures 88(Apr.1):

[5] Cui Liyun, Hu Guijuan, Pan Jianyun, et al. (2024) Enhancement mechanical performance of brick powder-cement mortar with bio-inspired material. Construction and Building Materials 432: 136397.https://doi.org/https://doi.org/10.1016/j.conbuildmat.2024.136397

[6] Cui Liyun, Xu Ying, Wang Liang, et al. (2024) Investigating the hydration characteristics of iron tailings powder cement mortar produced by the mortar substitution method. Journal of Building Engineering 81: 108100.https://doi.org/https://doi.org/10.1016/j.jobe.2023.108100

[7] U.Angst, M.Büchler (2015) On the applicability of the Stern-Geary relationship to determine instantaneous corrosion rates in macro-cell corrosion. Materials and Corrosion 66(10): 1017–1028.https://doi.org/https://doi.org/10.1002/maco.201407997

[8] Ji Yongsheng, Zhao Wen, Zhou Min, et al. (2013) Corrosion current distribution of macrocell and microcell of steel bar in concrete exposed to chloride environments. Construction and Building Materials 47(5): 104-110.https://doi.org/https://doi.org/10.1016/j.conbuildmat.2013.05.003

[9] Cao Chong (2014) 3D simulation of localized steel corrosion in chloride contaminated reinforced concrete. Construction and Building Materials 72: 434-443.https://doi.org/https://doi.org/10.1016/j.conbuildmat.2014.09.030

[10] Yu Bo, Liu Jianbo, Li Bing (2017) Improved numerical model for steel reinforcement corrosion in concrete considering influences of temperature and relative humidity. Construction and Building Materials 142: 175-186.https://doi.org/https://doi.org/10.1016/j.conbuildmat.2017.03.045

[11] Otieno M., Beushausen H., Alexander M. (2016) Chloride-induced corrosion of steel in cracked concrete-Part I: Experimental studies under accelerated and natural marine environments. Cement and Concrete Research 79: 373-385.https://doi.org/https://doi.org/10.1016/j.cemconres.2015.08.009

[12] Fang Xurui, Pan Zichao, Ma Rujin, et al. (2025) Electrochemical–chemical–mechanical phase field model for non-uniform corrosion-induced cracking considering the rust precipitation. Engineering with Computers.https://doi.org/https://doi.org/10.1007/s00366-025-02132-0

[13] Hussain Raja Rizwan (2011) Effect of moisture variation on oxygen consumption rate of corroding steel in chloride contaminated concrete. Cement and Concrete Composites 33(1): 154-161

[14] Tu Xi, Wu Ye (2023) Numerical analysis on corrosion and mechanical performance of shear stud connector in concrete. Construction and Building Materials 363: 129816.https://doi.org/https://doi.org/10.1016/j.conbuildmat.2022.129816

[15] Zhang Guoyi, Tian Ye, Jin Xianyu, et al. (2020) A self-balanced electrochemical model for corrosion of reinforcing steel bar in considering the micro-environments in concrete. Construction and Building Materials 254: 119116.https://doi.org/https://doi.org/10.1016/j.conbuildmat.2020.119116

[16] Jiang Jianhua, Yuan Yingshu (2013) Development and prediction strategy of steel corrosion rate in concrete under natural climate. Construction and Building Materials 44: 287-292.https://doi.org/https://doi.org/10.1016/j.conbuildmat.2013.03.033

[17] Lu Caifeng, Wang Wei, Li Qingtao, et al. (2018) Effects of micro-environmental climate on the carbonation depth and the pH value in fly ash concrete. Journal of Cleaner Production 181(APR.20): 309-317.https://doi.org/https://doi.org/10.1016/j.jclepro.2018.01.155

[18] Gawin D Koniorczyk M, Pesavento F (2013) Modelling of hydro-thermo-chemo-mechanical phenomena in building materials. Bulletin of the Polish Academy of Sciences Technical Sciences 61(1): 51-63

[19] Gawin Dariusz, Pesavento Francesco, Koniorczyk Marcin, et al. (2020) Poro-mechanical model of strain hysteresis due to cyclic water freezing in partially saturated porous media. International Journal of Solids and Structures 206: 322-339.https://doi.org/https://doi.org/10.1016/j.ijsolstr.2020.09.016

[20] Page C.L., Lambert P. (1987) Kinetics of oxygen diffusion in hardened cement pastes. Journal of Materials Science 22(3): 942-946.https://doi.org/https://doi.org/10.1007/bf01103534

[21] Rettich T. R., Battino R., Wilhelm E. (2000) Solubility of Gases in Liquids. 22. Highprecision Determination of Henry Constants for Oxygen in Liquid Water from T=274 to 328 K. Journal of Chemical Thermodynamics 32(9): 1145-1156

[22] Zhang Weiping, Chen Junyu, Luo Xujiang (2019) Effects of impressed current density on corrosion induced cracking of concrete cover. Construction and Building Materials (204): 213-223.https://doi.org/https://doi.org/10.1016/j.conbuildmat.2019.01.230

[23] Chen Jinwei, Fu Chuanqing, Ye Hailong, et al. (2020) Corrosion of steel embedded in mortar

and concrete under different electrolytic accelerated corrosion methods. Construction and Building Materials 241.https://doi.org/https://doi.org/10.1016/j.conbuildmat.2019.117971

[24] Zhao Yuxi, Zhang Xiaowen, Ding Hangjie, et al. (2016) Non-uniform distribution of a corrosion layer at a steel/concrete interface described by a Gaussian model. Corrosion Science 112: 1-12.https://doi.org/https://doi.org/10.1016/j.corsci.2016.06.021

[25] Tariku F., Kumaran K., Fazio P. (2010) Transient model for coupled heat, air and moisture transfer through multilayered porous media. International Journal of Heat & Mass Transfer 53(15-16): 3035-3044

[26] Gawin Dariusz, Pesavento Francesco, Schrefler Bernhard A. (2006) Hygro-thermo-chemo-mechanical modelling of concrete at early ages and beyond. Part I: Hydration and hygro-thermal phenomena. International Journal for Numerical Methods in Engineering 67(3): 299-331.https://doi.org/https://doi.org/10.1002/nme.1636

[27] Davie C. T., Pearce C. J., Bićanić N. (2006) Coupled Heat and Moisture Transport in Concrete at Elevated Temperatures-Effects of Capillary Pressure and Adsorbed Water. Numerical Heat Transfer Part A Applications 49(8): 733-763

[28] Du Mingyue.(2015). Thermo-hygro-mechanical model of early-age concrete based on micro-pore structure evolution. Zhejiang University.

[29] Kondepudi D.K., Prigogine I.(1998). Modern thermodynamics: from heat engines to dissipative structures. John Wiley & Sons.

[30] A.Baroghel.Bouny, A.M.Mainguy, Lassabatere B.T., et al. (1999) Characterization and identification of equilibrium and transfer moisture properties for ordinary and high-performance cementitious materials. Cement and Concrete Research 29(8): 1225-1238.https://doi.org/10.1016/S0008-8846(99)00102-7

[31] Tenchev R. T., Li L. Y., Purkiss J. A. (2001) Finite element analysis of coupled heat and moisture transfer in concrete subjected to fire. Numerical Heat Transfer: Applications 39(7): 685-710

[32] Gawin.D, Majorana C. E., A Schrefler.B. (1999) Numerical analysis of hygro-thermal behaviour and damage of concrete at high temperature. Mechanics of Cohesive-frictional Materials 4: 37-74

[33] Lewis RW Schrefler BA.(1998). The finite element method in the static and dynamic deformation and consolidation of porous media (2nd). Chichester: John Wiley & Sons.

[34] Cengel.Y.A.(1998). Heat transfer: a practical approach. New York: McGraw- Hill.

[35] Pour-Ghaz M., Isgor O. B., Ghods P. (2009) The effect of temperature on the corrosion of steel in concrete. Part 2: Model verification and parametric study. Corrosion Science 51(2): 426-433

[36] Zhang Guoyi, Tian Ye, Fu Chuanqing, et al. (2024) The impact of oxygen availability on steel corrosion considering the self-balance between anodic and cathodic corrosion cells. Corrosion Science 236: 112252.https://doi.org/https://doi.org/10.1016/j.corsci.2024.112252

[37] Greenberg A. E., Trussell R. Rhodes, Clesceri Lenore S, et al. (2005) Standard methods for the examination of water and wastewater : supplement to the sixteenth edition. American Journal of Public Health & the Nations Health 56(3): 387.https://doi.org/https://doi.org/10.2105/AJPH.56.4.684-a

[38] Ozbolt J., Balabanic G., Kuster M. (2011) 3D Numerical modelling of steel corrosion in concrete structures. Corrosion Science 53(12): 4166-4177.https://doi.org/https://doi.org/10.1016/j.corsci.2011.08.026

[39] Ababneh A., Benboudjema F., Xi Y. P. (2003) Chloride penetration in nonsaturated concrete. Journal of Materials in Civil Engineering 15(2): 183-191.https://doi.org/https://doi.org/10.1061/(asce)0899-1561(2003)15:2(183)

[40] Tang L., Nilsson L. O. (1993) Chloride binding capacity and binding isotherms of OPC pastes and mortars. Cement & Concrete Research 23(2): 247-253

[41] Ozaka Y., Fujiwara T., Akita H. (1997) A practical procedure for the analysis ofmoisture transfer within concrete due to drying. Magazine of Concrete Research 49(179): 129-137

[42] Ma Hongyan, Hou Dongshuai, Liu Jun, et al. (2014) Estimate the relative electrical conductivity of C-S-H gel from experimental results. Construction and Building Materials 71: 392-396.https://doi.org/https://doi.org/10.1016/j.conbuildmat.2014.08.036

[43] Baant Z. P., Najjar L. J. (1972) Nonlinear water diffusion in nonsaturated concrete. Materials and Structures 5(1): 3-20.https://doi.org/https://doi.org/10.1007/BF02479073

[44] Zhang Guoyi, Zhu Yifei, Lin Xingmin, et al. (2021) Numerical simulation of electrochemical mechanism of steel rebar corrosion in concrete under natural climate with time-varying temperature

and humidity. Construction and Building Materials 306: 124873.https://doi.org/https://doi.org/10.1016/j.conbuildmat.2021.124873

[45] Zhang Guoyi, Tian Ye, Zhao Ruoyi, et al. (2023) Dynamic self-balanced electrochemical model for non-uniform corrosion of steel reinforcement in concrete under combined effects of heat-moisture-chlorine-oxygen. Journal of Building Engineering 80: 108117.https://doi.org/https://doi.org/10.1016/j.jobe.2023.108117

[46]Hausmann D (1967) Steel corrosion in concrete-How does it occur? Materials Protection 6(11): 19-23

[47] Yu Bo, Liu Jianbo, Chen Zheng (2017) Probabilistic evaluation method for corrosion risk of steel reinforcement based on concrete resistivity. Construction and Building Materials 138: 101-113.https://doi.org/https://doi.org/10.1016/j.conbuildmat.2017.01.100

[48] Zhou Binbin, Gu Xianglin, Guo Hongyuan, et al. (2018) Polarization behavior of activated reinforcing steel bars in concrete under chloride environments. Construction and Building Materials 164: 877–887

[49] Zhang Guoyi, Tian Ye, Liu Yu, et al. (2024) Dynamic Electrochemical Model of Steel Corrosion in Concrete Microenvironment under Multifield Action of Heat-Moisture-Chlorine. Journal of Materials in Civil Engineering 36(1): 04023507

[50] Ann Ki Yong, Song Ha-Won (2007) Chloride threshold level for corrosion of steel in concrete. Corrosion Science 49(11): 4113-4133.https://doi.org/https://doi.org/10.1016/j.corsci.2007.05.007

[51] Muehlenkamp E. B., Koretsky M. D., Westall J. C. (2005) Effect of Moisture on the Spatial Uniformity of Cathodic Protection of Steel in Reinforced Concrete. Corrosion 61(6): 519-533

Appendix

The energy, moisture mass and dry air mass balance equations of concrete are shown in Eq.(A1)~(A3).

$$\begin{aligned}&(\rho C)_{eff}\frac{\partial T}{\partial t}-\nabla\cdot(\lambda\nabla T)-\left[\varepsilon_L\rho_L C_L\frac{\mathbf{K}K_L}{\mu_L}\nabla\left(P_G-P_C-\varepsilon_L\rho_L\mathbf{g}\right)\right]\cdot\nabla T\\&-\varepsilon_G\rho_G C_G\frac{\mathbf{K}K_G}{\mu_G}\left(\nabla P_G-\varepsilon_G\rho_G\mathbf{g}\right)\cdot\nabla T=-\dot{M}_{va}\Delta H_V\end{aligned}\tag{A1}$$

$$\begin{aligned}
&\left(\rho_L-\rho_V\right)\phi\left(\frac{\partial S}{\partial T}\frac{\partial T}{\partial t}+\frac{\partial S}{\partial P_C}\frac{\partial P_C}{\partial t}\right)-\nabla\cdot\left[\varepsilon_G\rho_G\frac{M_AM_V}{M_G{}^2}\mathbf{D}_G\nabla\left(\frac{P_V}{P_G}\right)\right]\\
&-\nabla\cdot\left[\varepsilon_L\rho_L\frac{\mathbf{K}K_L}{\mu_L}\nabla\left(P_G-P_C-\varepsilon_L\rho_L\mathbf{g}\right)\right]-\nabla\cdot\left[\varepsilon_G\rho_V\frac{\mathbf{K}K_G}{\mu_G}\left(\nabla P_G-\varepsilon_G\rho_G\mathbf{g}\right)\right]\\
&+\phi\left(1-S\right)\left(\frac{\partial\rho_V}{\partial T}\frac{\partial T}{\partial t}+\frac{\partial\rho_V}{\partial P_C}\frac{\partial P_C}{\partial t}\right)+\phi S\frac{\partial\rho_L}{\partial T}\frac{\partial T}{\partial t}=0
\end{aligned}\tag{A2}$$

$$\begin{aligned}
&\rho_A\phi\left(\frac{\partial S}{\partial T}\frac{\partial T}{\partial t}+\frac{\partial S}{\partial P_C}\frac{\partial P_C}{\partial t}\right)-\nabla\cdot\left[\varepsilon_G\rho_G\frac{M_AM_V}{M_G{}^2}\mathbf{D}_G\nabla\left(\frac{P_A}{P_G}\right)\right]\\
&-\nabla\cdot\left[\varepsilon_G\rho_A\frac{\mathbf{K}K_G}{\mu_G}\left(\nabla P_G-\varepsilon_G\rho_G\mathbf{g}\right)\right]+\phi\left(1-S\right)\left(\frac{\partial\rho_A}{\partial T}\frac{\partial T}{\partial t}+\frac{\partial\rho_A}{\partial P_G}\frac{\partial P_G}{\partial t}+\frac{\partial\rho_A}{\partial P_C}\frac{\partial P_C}{\partial t}\right)=0
\end{aligned}\tag{A3}$$